Hindawi
Advances in Civil Engineering
Volume 2020, Article ID 8818278, 16 pages
https://doi.org/10.1155/2020/8818278

Research Article

Infrared Temperature Law and Deformation Monitoring of Layered Bedding Rock Slope under Static Load

Zhigang Tao,[1,2] **Kuiming Liu**,[1,2] **Xuebin Cui**,[1,2] **Xiaobing Qiao**,[3] **and Xiaoming Sun**[1,2]

[1]*State Key Laboratory for Geomechanics & Deep Underground Engineering, China University of Mining & Technology (Beijing), Beijing 100083, China*
[2]*School of Mechanics and Civil Engineering, China University of Mining & Technology (Beijing), Beijing 100083, China*
[3]*Gansu Province Highway Aviation Tourism Investment Group Co., Ltd., Gansu 730030, China*

Correspondence should be addressed to Zhigang Tao; taozhigang@263.net

Received 15 July 2020; Revised 7 November 2020; Accepted 23 November 2020; Published 21 December 2020

Academic Editor: Doo-Yeol Yoo

China is a mountainous and hilly country with frequent large-scale landslides with complicated mechanisms and serious damage. The layered rock slopes have the worst stability, undergo the most serious damage, and have been rarely investigated due to limitations of measurement methods and instruments. Taking the Nanfen open-pit iron mine as an example, a physical large-model similarity ratio test system is used to simulate the landslide remote monitoring process. The development of the sliding surface, stress-strain characteristics, and infrared law of the bedded rock slope are analyzed. Results show that the anchor cable with constant resistance and large deformation plays a significant role in the stability of the slope, and its maximum slip force is 420 N and 630 N, respectively. Slip and crack are the main mechanisms of energy release in layered rock slope. Some scheme improvement measures for this kind of test are put forward, which provides basis and optimization scheme for the subsequent study of layered rock slope.

1. Introduction

Slope stability monitoring [1–13] and evaluation is a new emerging landslide hazard prediction and control technique, which has great research significance for landslide prevention and control. With the increasing economic strength of China, the construction of large-scale projects [14] has attracted worldwide attention. Along with the implementation of the national strategic plan, including the "one belt along the road" and "Yangtze River Economic Belt," construction problems in the southwest mountainous area have become the top priority. The number of landslides is increasing each year, which seriously affects the construction and operational safety of the project [15]. Almost all mountainous areas with human habitation and engineering activities in China will suffer from landslides, which have become the most frequent and costly type of geological disaster [16–18]. Large scale landslides and giant landslides occur frequently in China, especially in western China. However, layered rock slopes [19–21] commonly have the worst stability and greatest damage. Engineering practice shows that the bedded slopes easily incur large-scale deformation. Once an instability damage occurs, it will seriously hinder construction progress, threaten safety, and seriously damage property [22].

The landslides are characterized by large scale, complex mechanism, and serious damage, which have attracted the attention of scientists all over the world [23] and have produced rich research results. For example, the "advance warning and monitoring system" developed by Zan et al. [24] can automatically monitor vibrations, pore water pressure, surface displacement, rainfall, and other parameters in the landslide body and automatically trigger the alarm program to send out the landslide disaster warning; Reevea et al. [25] used In-SAR technology to monitor rock slopes in open-pit mines to evaluate the slope stability where frequent collapses occur in order to judge the slope stability. Ohbayashi et al. [26] proposed a "perceptual node network system" to monitor deformation inside a landslide body. The system has self-recovery, automatic control, and efficient

data transmission to avoid damage to the sensing device caused by natural disasters. Tang et al. [27] conducted theoretical and experimental studies on the time-domain reflection method and its application in landslide monitoring. Zhang et al. [28] used Zig Bee communication methods and wireless sensor network technology to establish standardized landslide disaster prediction methods and early warning models to achieve uninterrupted dynamic monitoring of sliding force and anti-sliding force. They want to go deeper into the slope and essentially realize remote monitoring and early warning of landslide disasters.

In summary, these monitoring and control methods have laid a theoretical and practical basis for the analysis and evaluation of slope stability. In order to analyze the stress-strain law and infrared characteristics of bedded slopes under static load, and make up for the shortage of research results of stress-strain characteristics of this kind of slope restricted by measurement methods and instruments [29], we used physical models [30–40] to simulate and reproduce the remote monitoring process of the Nanfen open-pit iron mine landslide in order to better understand the deformation characteristics.

2. Project Summary

2.1. Engineering Survey. Nanfen open-pit iron ore mine is located in the Taizihe sag in the northern margin of the Liaodongtai anticline in the Yingkou–Kuandian uplift in the North China Platform. The monoclinic ore body, the largest in Asia, is located in the iron-bearing section of the Archean Anshan Group. The monomer open-pit iron ore mine currently has an annual production capacity of 13 million *t*/*a* of iron ore.

Due to the complex engineering geological conditions, the development of joints, the accumulation of boulders on the slope surface, and the influence of blasting and excavation, the lower slope of the Nanfen open-pit iron mine did not rely on design requirements. In order to increase the anti-sliding force of the old landslide body and improve slope stability, the platform at the southern end of the lower slope of the stope is 394 m and below. The stope slope with a strike of 294° forms a bulge near the No. 12 exploration line, forming a convex slope, which acts as a counter-pressure slope to enhance the slope stability (Figure 1).

2.2. Topographic Features. The Nanfen open pit iron mine is primarily a monoclinic structure composed of metamorphic strata. The mountain ranges are oriented east-west, with steep valley and sparse vegetation. Generally, the elevation of the mountain ranges is 500–600 m, and the relative height is 300–400 m. The elevation of the Huangbaiyu river bed in the southern mining area is 327 m, and the elevation of the Miao'ergou River in the northern mining area is 296 m. The stope is 3 km long from north to south and 1.5 km wide from east to west. The east side of the stope is a single-sloping structure, and the west side of the stope is a monoclinic structure (Figure 2).

2.3. Stratigraphic Lithology. The Anshan Group is widely developed in the Nanfen open-pit mine, followed by the Paleozoic Liaohe Group, Sinian strata, and Quaternary strata:

(1) The Dagugou Formation in the Archean Anshan Group can be divided into five members. Mining is primarily conducted in the second, third, and fourth rock members (Table 1).

(2) The Yuan Liaohe Group is not integrated into the Anshan Group and is primarily composed of quartzite, phyllite, and marble, with a thickness of 670 m. The Yuan Liaohe Group is distributed in the middle and north of the mining area.

(3) Sinian strata are unconformably covered by the Liaohe Group and form a fault contact with the Anshan Group. Sinian strata are primarily composed of quartzite and shale and are distributed in the western part of the mining area.

2.4. Regional Geologic Structure. The mining area is located on the southern edge of Taizihe depression, which has a peninsula-like shape. Geologic structures present within the area include faults and folds, primarily NNE-trending major faults and reverse anticlines.

Fractures have different properties depending on orientation. The NNE compressive fractures play a key role in iron ore storage and a certain destructive role in iron ore formation but, more importantly, provide significant ore storage. Folds are primarily anticlinal domes. The anticline in the open-pit mine is located in the southwest wing of the Heibeishan reverse Anticline. The anticline is folds Sinian strata with the Qidashan gneiss complex in the core of the anticline. The axis of the elliptical dome is close to N–S, and its dip angle is 30°. The Qidashan gneissic complex is developed in its core, and its dip angle is 40°.

2.5. Joint Development Characteristics. The lower slope of the Nanfen open-pit iron ore mining site is cut by 5–6 joints sets. These joints sets do not have a significant influence on slope stability. Their main function is to reduce overall strength of the rock mass. Two joints sets located in the lower gang have a significant influence on slope stability.

(1) First-order joints have an average orientation of 295°/48°. Joint surfaces have sliding marks, and the joint roughness coefficient is approximately 2–4. Joints in this group significantly penetrate the slope and constitute the main slip surface for landslides in the lower plate.

(2) Secondary joints have an average orientation of 291°/13°. These joints are widely distributed and have a small dip angle. Secondary joints commonly are traces of water flow in the exposed joints. Because the secondary joints are inclined toward the pit and are exposed on the slope surface, they may form the lower sliding surface of a landslide (Figure 3).

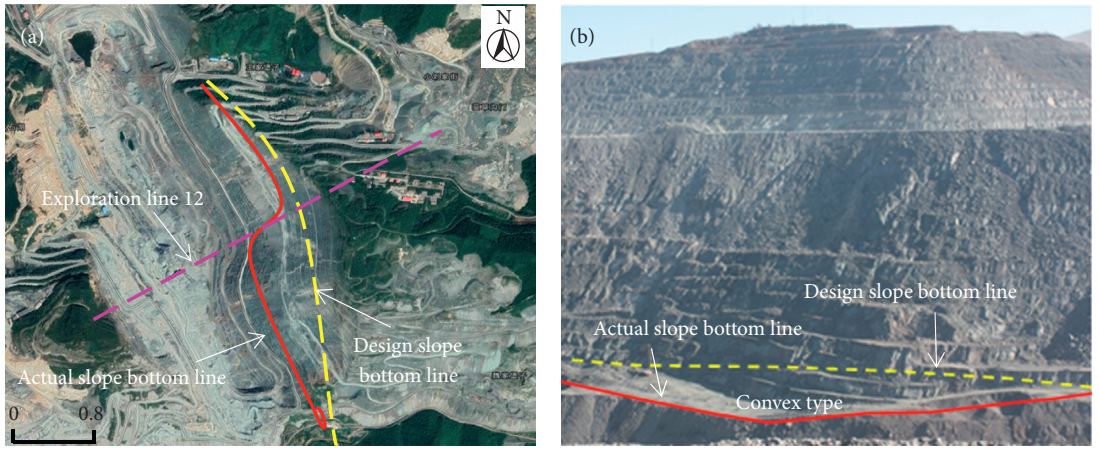

Figure 1: Images showing the convex slope. (a) Satellite imagery (N41° E123°). (b) Entity diagram.

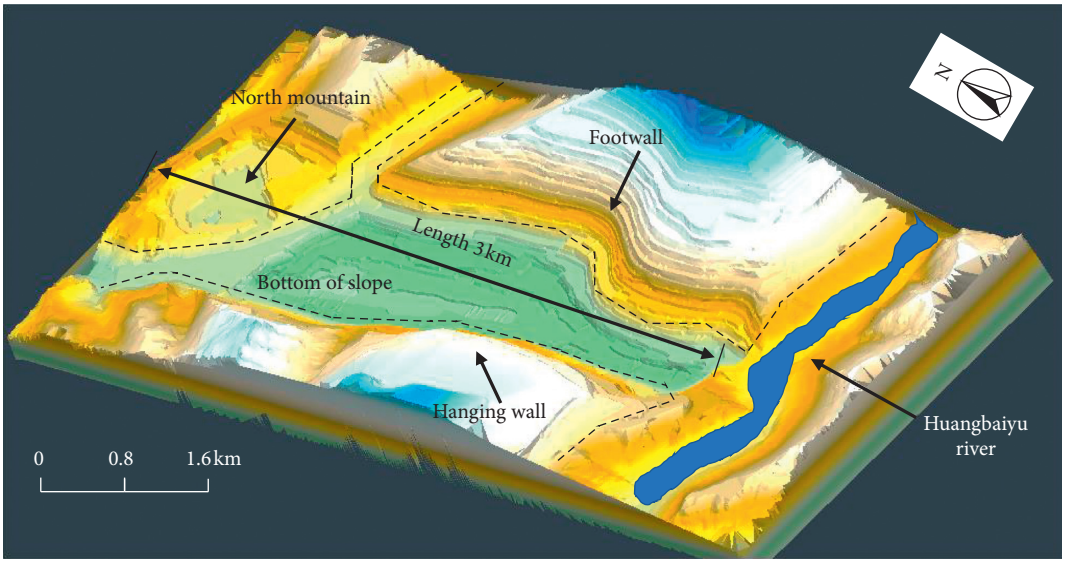

Figure 2: Mine mining site shape and landform.

Table 1: Characteristics of typical rock sections of the Dagugou Formation.

Rock section	Rock section name	Lithological composition	Thickness (m)	Distribution characteristics
Second	Schist section	Composition of amphibolite schist, mica feldspar quartz schist and mica quartz schist	500	East of the mining area, from Heibeigou to Tieshan
Third	Iron-bearing rock section	Green curtain angle flash (slice) rock and magnet quartzite, quartz green mud schist, iron ore layer and black cloud green mud schist	350	Chaxingou to Huangbai gully, integrated on the schist
Fourth	Mica quartz schist section	Integrated on the third layer of iron	40–100	South of Miaoergou–Huangbaiyu

3. Test System Composition and Test Method Design

3.1. Test Host System. In this experiment, the physical large-model similarity test system independently developed by the China University of Mining and Technology (Beijing) was used to reproduce the whole process of remote monitoring of Nanfen open-pit iron mine landslide. The system consists of two parts: the main engine and the hydraulic control system.

(1) The main engine has a frame composed of four load-bearing beams, screw nuts, and connecting plates (Figure 4). On each side of each load-bearing beam,

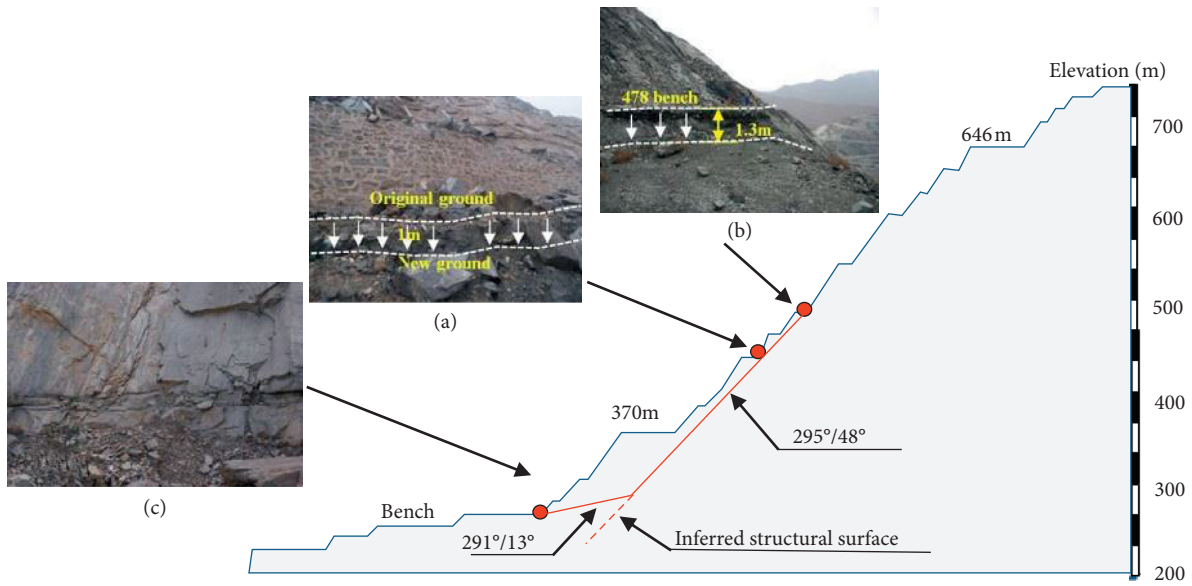

Figure 3: Images showing two sets of joints in the footwall at the Nanfen open-pit iron mine. (a) The failure characteristic on the top of bench with an elevation of 478 m, and the attitude of structural surface is 295°/48°. (b) The failure characteristic on the top of bench with an elevation of 430 m. (c) Structural surface exposed on the bottom of the bench with an elevation of 274 m, and the attitude of structural surface is 291°/13°.

six pairs of uniform pressure loaders are installed to apply loads to the test model. On both sides of the frame, seven pairs of side limiting beams are symmetrically mounted to limit lateral deformation in the model. The center positions of both ends of the frame are equipped with plane rotation bearing shafts, respectively, located on two plane rotation bearings, which are fixed to the ground fixed plate using bolts.

The main technical attributes of the model include a model block size of 160 cm (length) × 160 cm (width) × 40 cm (height); a one-way load, two-way load, or step load can be applied to the model, and the model can be tested under plane strain and quasi plane strain conditions. The maximum load concentration at the model boundary is 5 MPa, the load concentration deviation is less than 1%, the uniform range of the strain field of the model block can reach 130 × 130 cm, and the relative deviation of uniformity is less than 5%. The maximum cavity size in the model block is 60 cm; the model boundary load can be maintained for more than 48 hours; the total weight of main engine is 12700 kg (including uniform pressure loader); the maximum dimensions of the main engine are 3310 mm (length) × 970 mm (width) × 3010 mm (height).

(2) The hydraulic control system controls the loading of the test model and is primarily composed of 24 uniformly distributed pressure loaders, four rotating oil cylinders, high-pressure hoses, hydraulic regulators, and electric oil pumps (Figure 4). The input end of the regulators is connected to the electric oil pump, and the output end is divided into 8 groups, which are connected to the uniformly distributed pressure loaders and rotating oil cylinders. In order to ensure oil pressure stability, an argon cylinder is connected to the pressurizer.

The hydraulic control system has a total weight of 300 kg and a size of 1950 mm (length) × 840 mm (width) × 1570 mm (height). The electric oil pump has a total weight of 80 kg and a size of 800 mm (length) × 450 mm (width) × 900 mm (height). The motor has power and voltage ratings of 2.2 kW and 380 V, respectively.

3.2. Testing System

3.2.1. Strain Test System. The big data acquisition system is a special instrument for collecting and processing strain test data in the vicinity of the sliding surface during the test. This system employs DH3818 static strain test system, which consists of a data acquisition box, microcomputer, and support software. The system can automatically, accurately, reliably, and quickly measure static strain stress values at multiple points in large structures, models, and material stress tests.

The DH3818 static strain test system has external dimensions of 353 mm (length) × 291 mm (width) × 105 mm (height), a sampling rate in the programmed state of 10 measuring points/second, a test strain range of ±19999 $\mu\varepsilon$, a resolution of 1 $\mu\varepsilon$, an uncertainty in the program-controlled system of less than 0.5% ± 3 $\mu\varepsilon$, zero drift ≤4 $\mu\varepsilon$/2 h in the programmed state, a range of auto balance within ±15000 $\mu\varepsilon$, and an error of resistance value for strain gauges with a sensitivity coefficient $k = 2120\,\Omega$ of 1.5%. The correction coefficient of the measured result in the manual state ranges

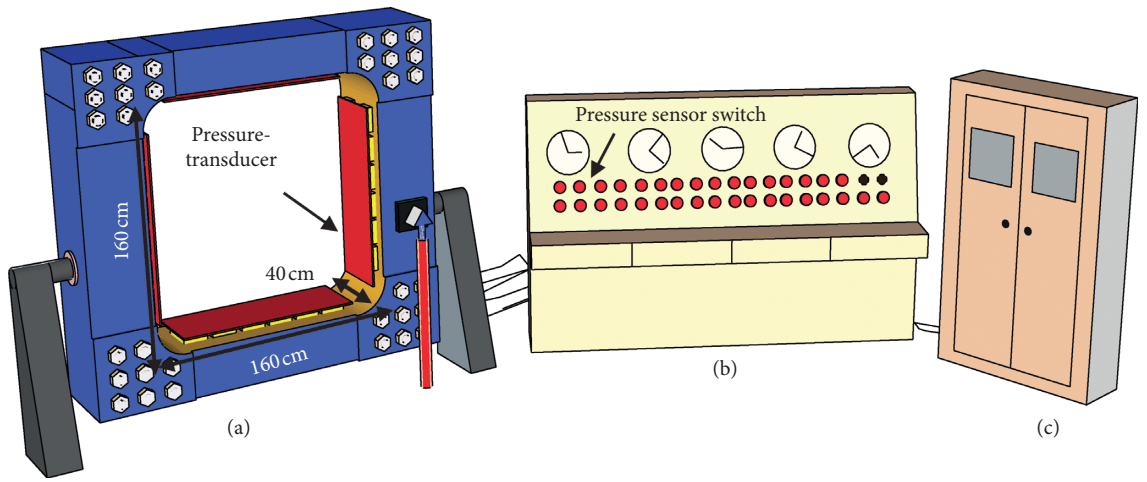

Figure 4: Schematic diagram of the main engine and hydraulic control system. (a) Main engine. (b) Work station. (c) Nitrogen gas bottle.

from 0.0000 to 0.9999. The power supply voltage is 220 V ± 10%, 50 Hz ± 1%. Each static strain gauge can measure up to 20 points, and each computer controls ten static strain gauges.

In this test, 28 strain gauges are installed on both sides of the sliding surface within 20 mm. The strain gauges are 164 mm apart and distributed on both sides of the sliding surface with a length of 1318 mm. The single strain gauges are connected by connecting wires (Figure 5).

3.2.2. Displacement Test System. The displacement test system is a special instrument for collecting and processing displacement test data from the top surface of the landslide body during the test. This experiment uses a YHD-50 displacement meter produced by Liyang Jiangnan Electronic Instrument factory (Figure 6).

The YHD-50 displacement meter has a range of 5 cm, measurement accuracy of 0.005 mm, and a working temperature range of −35°C–60°C. The relative humidity is less than 90%, and the bridge mode is half bridge.

Four displacement sensors are, respectively, installed on top of the landslide body to collect and process surface displacement data from the top of the landslide body. The setting interval of the displacement meter is 206 mm (Figure 6).

3.2.3. Sliding Force Test System. In the sliding for test, two high-precision sliding force sensors are installed at the end of the anchor cables. The upper part of the sliding body is sensor 1, and the lower part of the sliding body is sensor 2. Steel wire rope (1 × 7) with the same rigidity instead of constant resistance communication cable is used to collect and process the sliding force data. The incident angle of fine steel wire is 25°, and the length is 642 mm (Figure 7).

The fine steel wire is installed by pre-drilling holes in the gypsum unit board. First, the angle of incidence of the steel wire is calculated; then, the holes are drilled (drilling diameter φ 10 mm). Next, the gypsum unit plates are stacked in the corresponding positions to check whether the axes of the holes line up; finally, the thin steel wire is passed through the hole and fixed to the loading frame (Figure 8).

4. Model Construction and Physical Simulation Test Analysis

4.1. Test Material. The test was carried out using a gypsum board with a water-paste ratio of 1 : 1. The physical properties of the material are shown in Table 2.

4.2. Physical Model Design. Based on the principle of sliding force remote monitoring, the ultimate mechanical balance principle is used to establish the functional relationship between the artificial mechanical system and the natural mechanical system. Figure 9 shows the physical model of the landslide body, which makes the following assumptions:

(1) The landslide body is regarded as a rigid body; that is, the landslide body itself does not have tensile or compression deformation during the landslide.

(2) The sliding surface is a plane.

(3) The length of the sliding surface is far greater than the depth of the sliding body, and the thrust above the top surface of the sliding body and the blocking force at the toe are ignored.

(4) The sliding force and anti-sliding force on the sliding surface are parallel to the sliding surface.

(5) The additional forces acting on the landslide, such as seismic force, engineering blasting, hydrostatic pressure, buoyancy, and hydrodynamic pressure, are not considered.

(6) The parameters of slope stability influence coefficient are as follows:

(a) Geometric influence coefficient: $\alpha = 26.6°$; $\theta = 25°$, $l = 1318$ mm, $v = 0.127\ m^3$, h (slope height): 810 mm, l (top width): 825 mm.

(b) Lithology influence coefficient: $\varphi = 23.59°$, $C = 36.35$ kpa, $\gamma = \rho\ g = 11.25\ kn/m^3$.

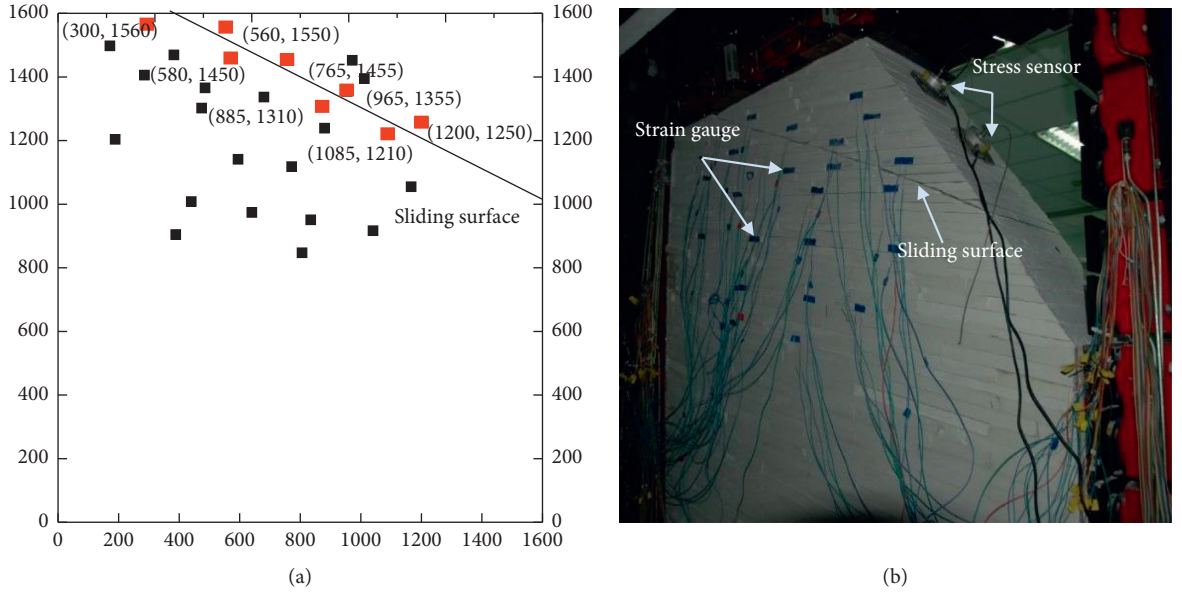

Figure 5: Image showing the solid position of the strain gauges.

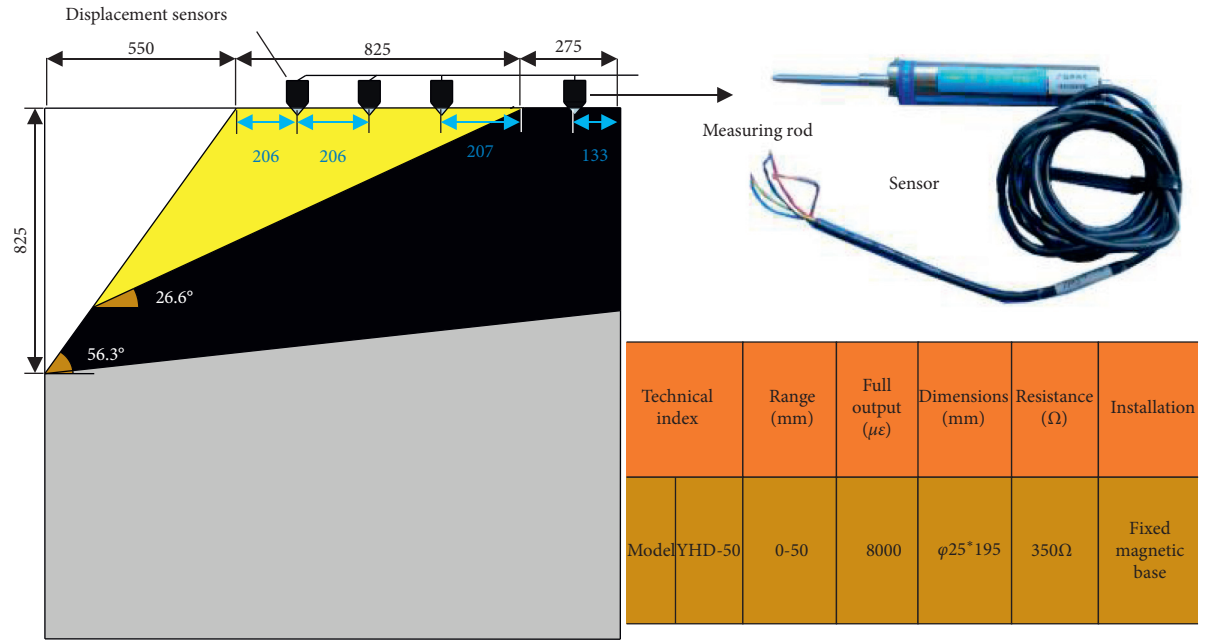

Technical index		Range (mm)	Full output ($\mu\varepsilon$)	Dimensions (mm)	Resistance (Ω)	Installation
Model	YHD-50	0-50	8000	φ25*195	350Ω	Fixed magnetic base

Figure 6: Schematic diagram of the displacement meter position.

4.3. Mechanical Model Design. According to the limit equilibrium principle, the force components of P, G, and F along the direction of the slip surface and perpendicular to the direction of the slip surface can be, respectively, obtained (Figure 10):

$$G_t + F_t = P \cdot [\cos(\alpha + \theta) + \sin(\alpha + \theta) \cdot \tan\overline{\varphi}] + (G + F)\tan\overline{\varphi} + c \cdot l, \quad (1)$$

$F_s = G_t + F_t$; F_s indicates the amount of sliding force on the sliding surface.

Then,

$$F_s = P \cdot [\cos(\alpha + \theta) + \sin(\alpha + \theta) \cdot \tan\overline{\varphi}] + (G + F)\cos\alpha \cdot \tan\overline{\varphi} + c \cdot l, \quad (2)$$

and $k_1 = \cos(\alpha + \theta) + \sin(\alpha + \theta) \cdot \tan\overline{\varphi}$ $k_2 = (G + F)\cos\alpha \cdot \tan\overline{\varphi} + c \cdot l$.

Then,

$$F_s = k_1 \cdot P + k_2, \quad (3)$$

where $\overline{\varphi}$ is the weighted average value of internal friction angle of each soil layer of the slope (°); c is the weighted

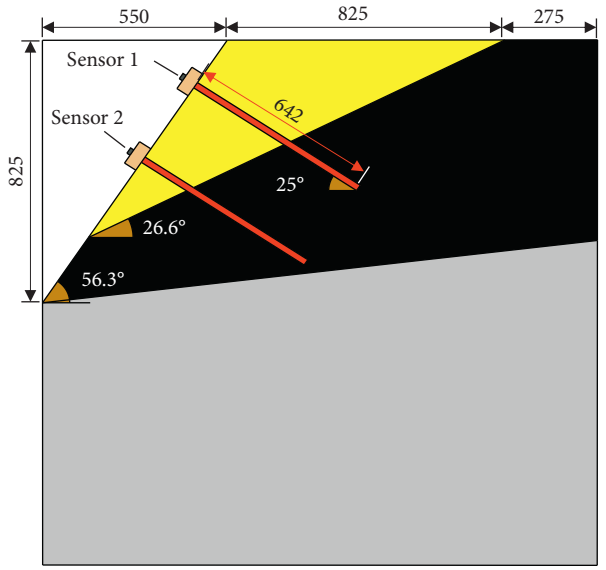

Figure 7: Schematic diagram showing the sliding force sensor.

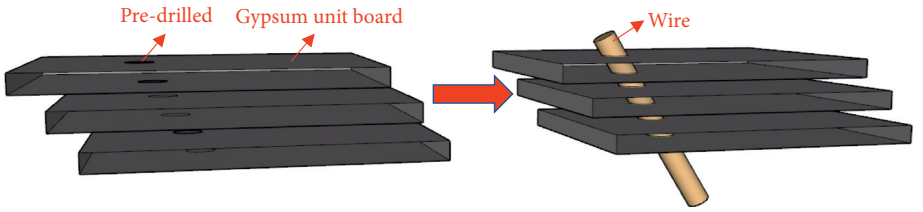

Figure 8: Schematic diagram showing the installation of the force sensor.

Table 2: Mudstone material physical parameters.

Lithology	Bulk weight (kN/m^3)	Uniaxial compressive strength (MPa)	Modulus of elasticity (GPa)	Poisson's ratio
Protolith	25.78	43.78	21.01	0.13
Simulated materials	9.72	4.50	0.94	0.32

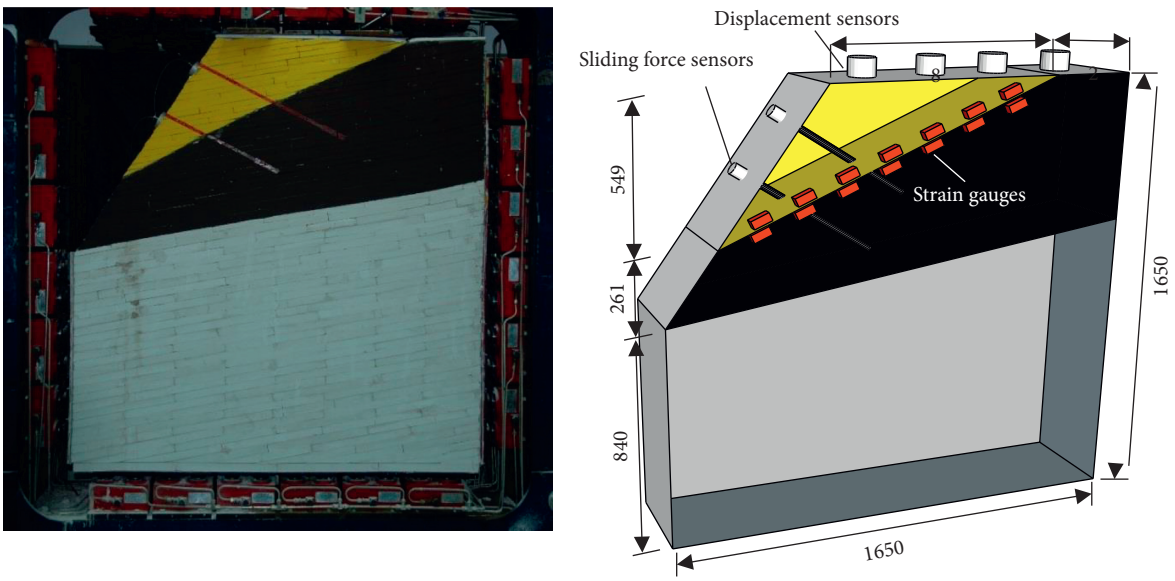

(a) (b)

Figure 9: Image and schematic diagram of the physical model.

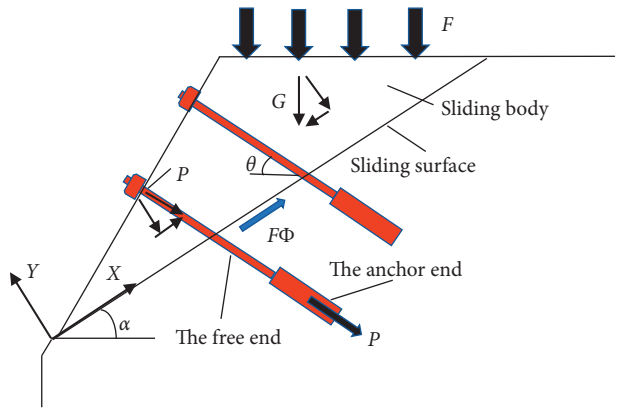

Figure 10: Schematic diagram of the mechanical model.

average cohesion of each soil layer on the sliding surface/kPa; and l is the length of sliding surface/*m*.

Equation (3) expresses the functional relationship between the artificial mechanical system and the natural mechanical system in the limit equilibrium state, that is, the functional relationship between the natural sliding force and the disturbing force P.

4.4. Loading Process Design. This test was carried out in a step-by-step manner. The first three loads were loaded every half an hour with an increase of 0.2 MPa each time, and the fourth load was loaded after 35 minutes with an increase of 0.4 MPa. The total test duration was 95 minutes (Table 3).

4.5. Test Process and Test Result Analysis

4.5.1. Displacement and Sliding Force Time Curve. The sliding force and displacement of the first point and the second point reach the maximum value after the fourth-stage load (1.1 MPa) is applied, and the failure occurs (Figure 11).

4.5.2. Loading Corresponding Images at Each Level. The loading map of each level is stable after loading for one minute at each level. The first stage loading change is small, and cracks start to appear after the second-stage loading. Cracks after the third-stage loading are more obvious than in the second level. After the fourth stage is loaded, the sliding body begins to break (Figure 12).

4.6. Strain Cloud

4.6.1. Pre-Load Strain Cloud Map. After the physical model has been set up for a period of time, it is in a stable state and there is no abnormal sound (Figure 13).

4.6.2. The First Loading Stage Strain Cloud Map. After the first loading stage is stabilized, displacement in the *X* and Y directions increases but not significantly. The landslide body has no visible deformation characteristics, and there is a sound at the top plate (Figure 14).

4.6.3. The Second Loading Stage Strain Cloud Map. After the second loading stage is stabilized, the strain cloud diagram shows that the internal strain of the sliding body does not significantly change (Figure 15). Some new small cracks are generated in the sliding body during secondary loading, and local crack propagation occurs.

4.6.4. The Third Loading Stage Strain Cloud Map. After the third loading stage is stabilized, the displacement inside the sliding body continues to increase, but there is still no substantial change. The sliding body does not produce significant slip, but cracks in its interior and surface continue to expand (Figure 16).

4.6.5. The Fourth Loading Stage Strain Cloud Map. After the fourth loading stage is stabilized, the model has produced large cracks, the sliding body recorded large relative slip along the sliding surface, and the anchor cable has undergone significant deformation. From the *X*, *Y* direction displacement cloud map, the previous load has changed significantly, and the model is destroyed (Figure 17).

4.7. Strain-Time Curve at Key Points

4.7.1. The Horizontal Strain versus Time Curve at Each Key Point. The first, second, and third key points do not change significantly with time, while the 17th and 18th key points change significantly with time (Figure 18).

4.7.2. The Vertical Strain at Each Key Point Changes with Time. The vertical displacement of key points 2, 3, and 17 changes little with time, while the vertical displacement of key points 1 and 18 significantly changes with time, and the change at key point 1 is more obvious than that at key point 18 (Figure 19).

In summary, it can be concluded that the displacement change at key point 18 positively correlates with time.

Note: strain gauges 81–90 were damaged during preloading, so there are only five key points of strain versus time as shown.

Table 3: Stress loading table.

Time	Loading level	Actual loading stress (MPa)	Corresponding instrument loading stress (MPa)
18 : 35	First	0.3	1.2
19 : 05	Second	0.5	2.0
19 : 35	Third	0.7	2.8
20 : 05	Fourth	1.1	4.4

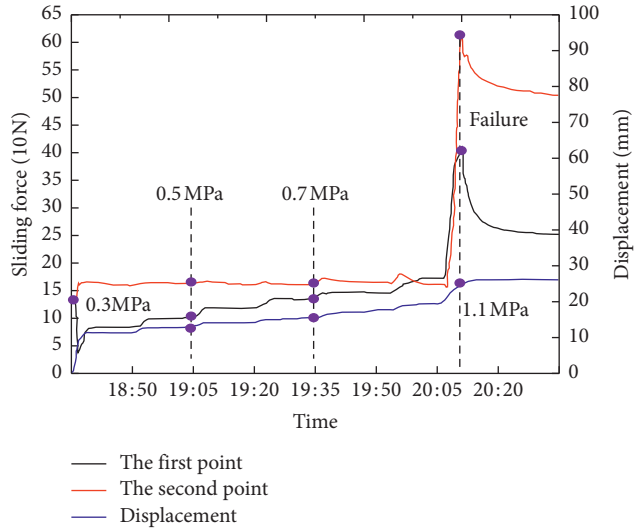

Figure 11: Displacement and sliding force time curve.

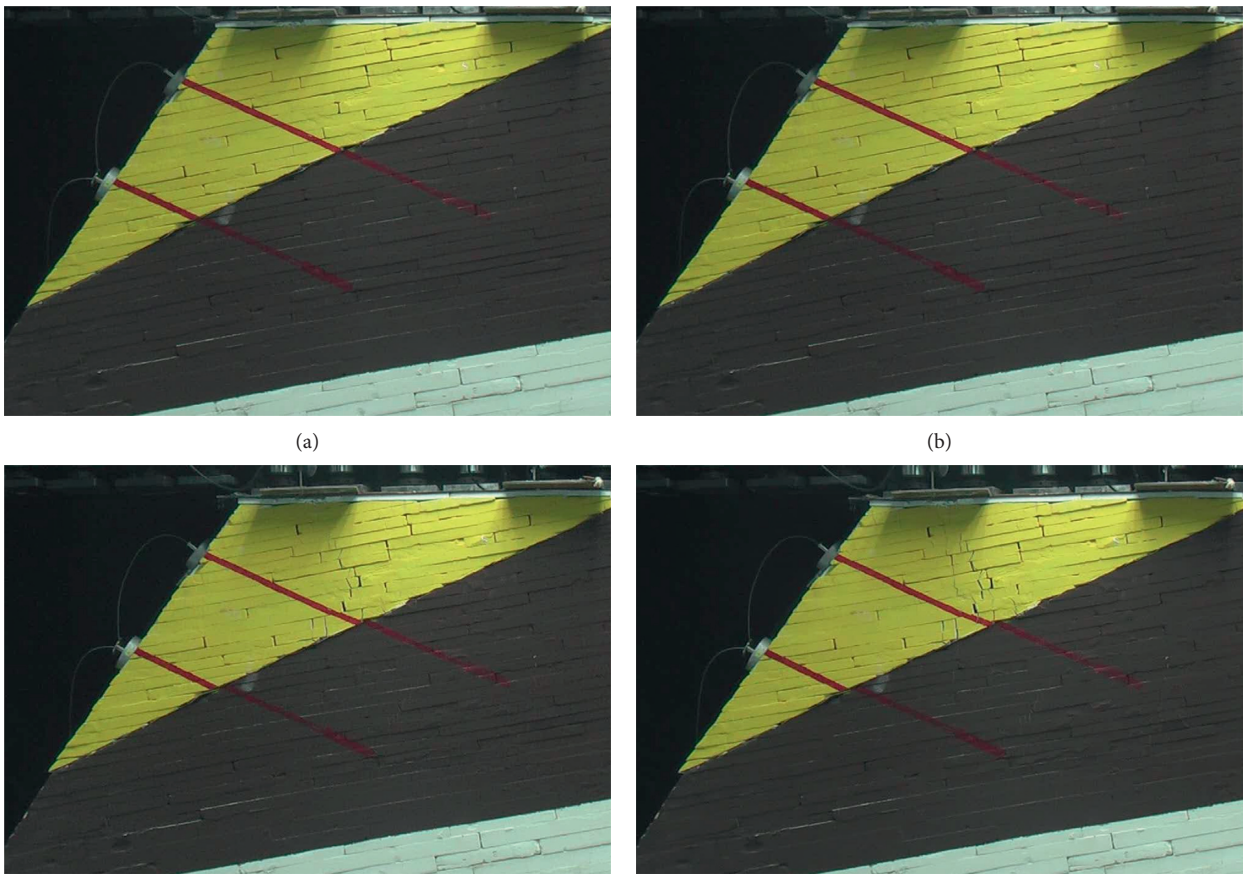

Figure 12: Continued.

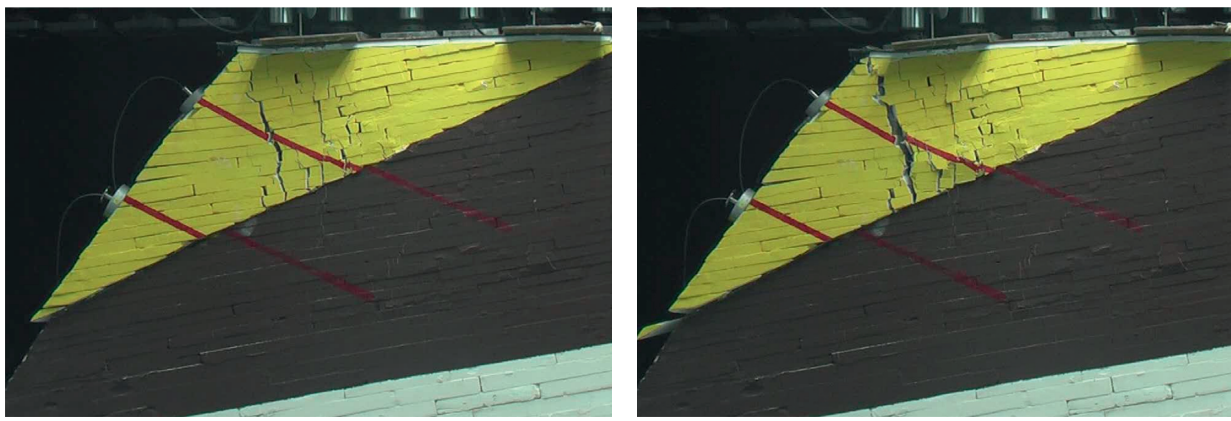

(e) (f)

Figure 12: Images of the model after loading and stabilization at all levels. (a) Before loading. (b) Level 1 load (0.3 MPa). (c) Level 2 load (0.5 MPa). (d) Level 3 load (0.7 MPa). (e) Level 4 load (1.1 MPa). (f) After destruction.

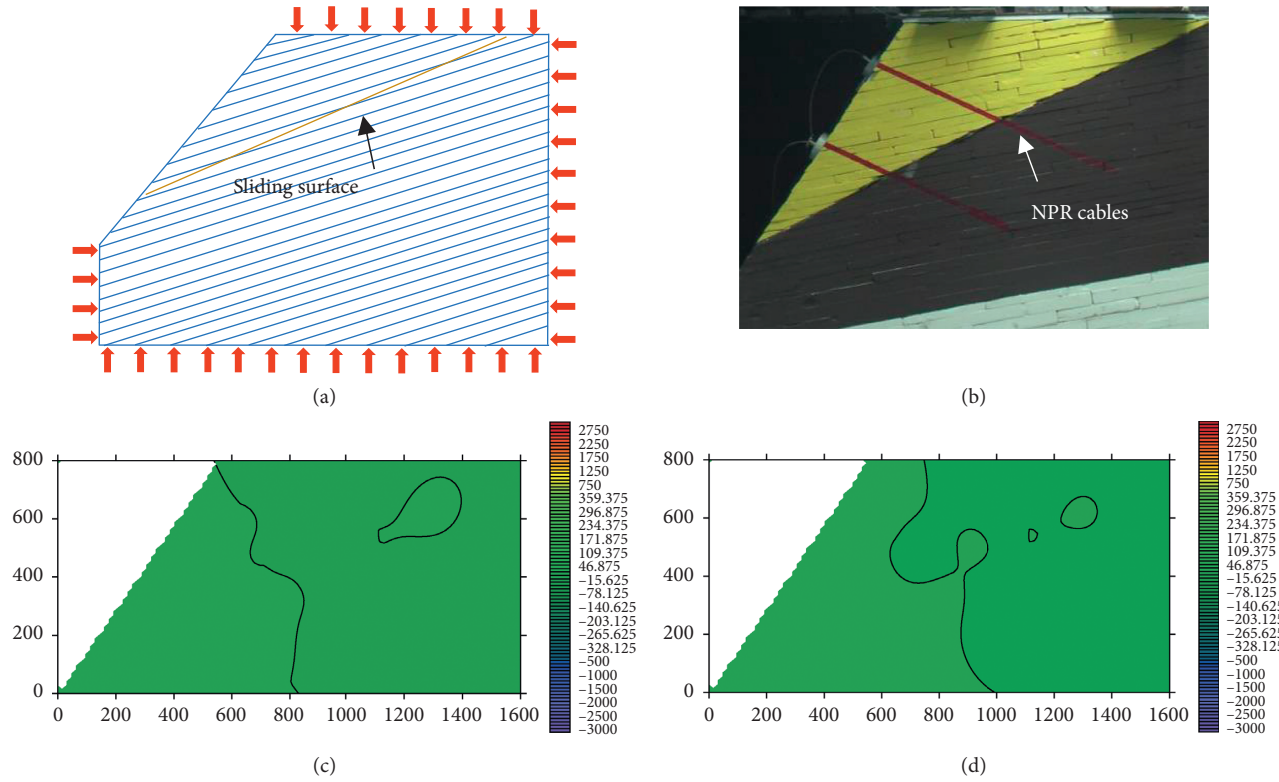

Figure 13: Pre-load strain cloud data. (a) Model loading diagram. (b) Model loading variation diagram. (c) X-directional strain cloud map. (d) Y-directional strain cloud map.

4.8. Infrared Temperature Curve. In the first loading stage (0.3 MPa), the gypsum board unit bodies of the sliding body are slowly pressed together, and the contact surfaces generate mutual friction (Figure 20). The interaction force between the loaded cell plates is transformed into deformation energy, which begins to gradually aggregate. The maximum concentration energy is found at E2 (35.5°C), and loading in the first phase increases the temperature by E2 − E1 = 1.0°C. When the energy is concentrated to the maximum value, the sliding body begins to produce a discontinuous sliding surface, the sliding body begins to partially slide, the released energy is approximately equal to the initial energy (i.e., $Q1 \approx Q2$), and the temperature is 34.5°C. At this time, stage II loading (0.5 MPa) is carried out. Since the first loading leads to higher energy concentration ($Q1$ is larger), the energy after the second loading will not reach the previous peak, and the highest infrared temperature is at E4

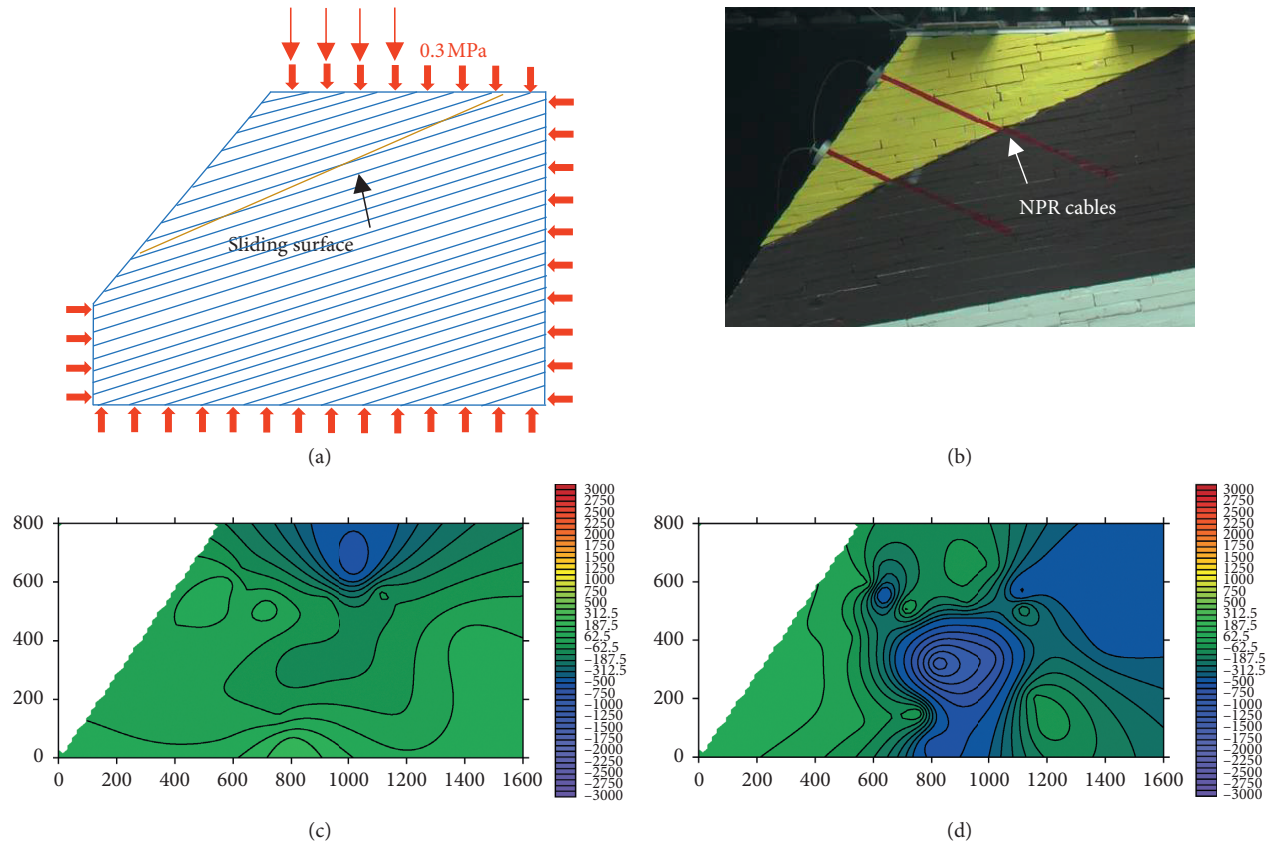

Figure 14: First loading stage stable strain cloud map. (a) Model loading diagram. (b) Model loading variation diagram. (c) X-directional strain cloud map. (d) Y-directional strain cloud map.

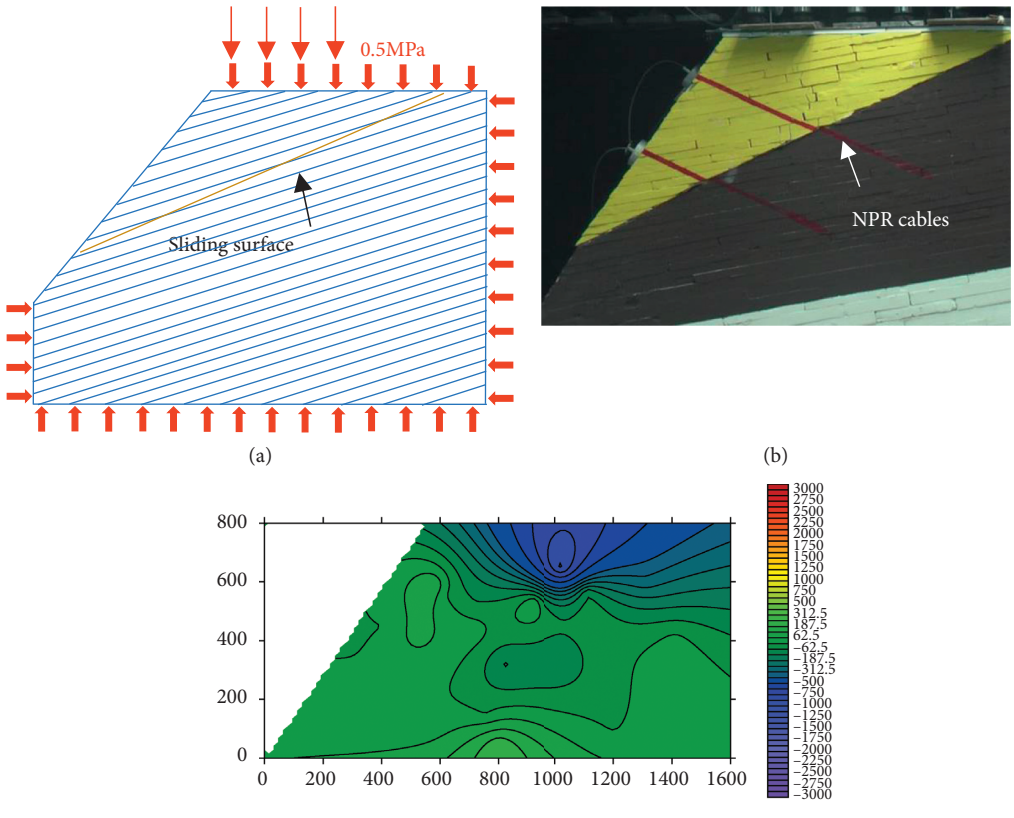

Figure 15: Continued.

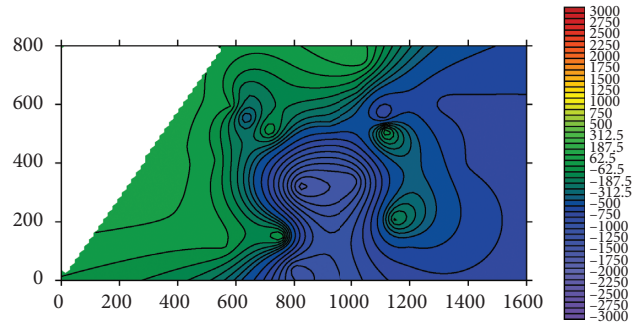

(d)

Figure 15: Second loading stage stable strain cloud map. (a) Model loading diagram. (b) Model loading variation diagram. (c) X-directional strain cloud map. (d) Y-directional strain cloud map.

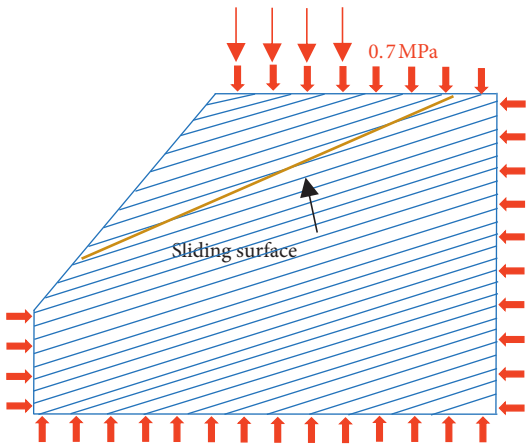

(a)

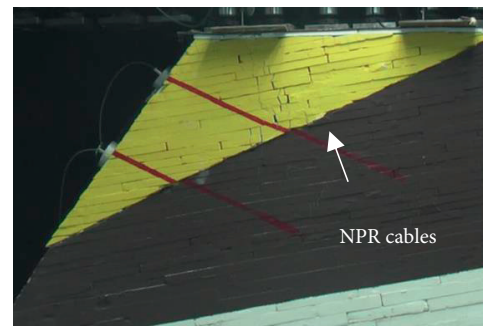

(b)

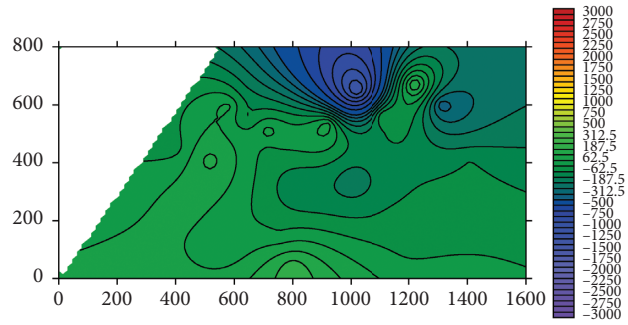

(c)

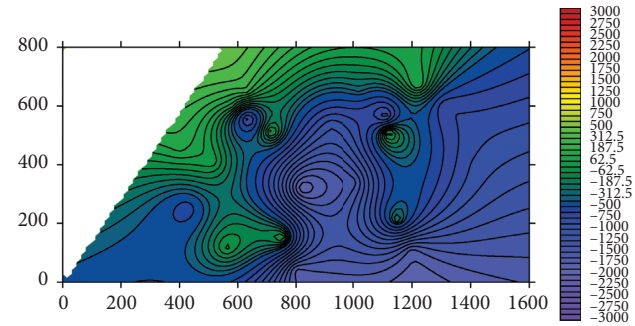

(d)

Figure 16: Third loading stage stable strain cloud map. (a) Model loading diagram. (b) Model loading variation diagram. (c) X-directional strain cloud map. (d) Y-directional strain cloud map.

(34.7°). After loading for a period of time, stage II loading no longer produces an agglomeration of energy, and the temperature rises by E4 − E3 = 0.2°C. At this point, the sliding surface inside the sliding body begins to expand gradually, and energy is released again. The released energy is still roughly equivalent to the energy of the loading and accumulation; that is, $Q3 \approx Q4$. After the second loading stage has stabilized for 30 minutes, the stage III loading (0.7 MPa) is started. The temperature no longer changes significantly with the loading time but fluctuates up and down around the temperature 34.5° before the third loading stage ($E5 \approx E6$). The energy inside the landslide body also changes like this. This is because, with increasing load, the sliding surface in the sliding

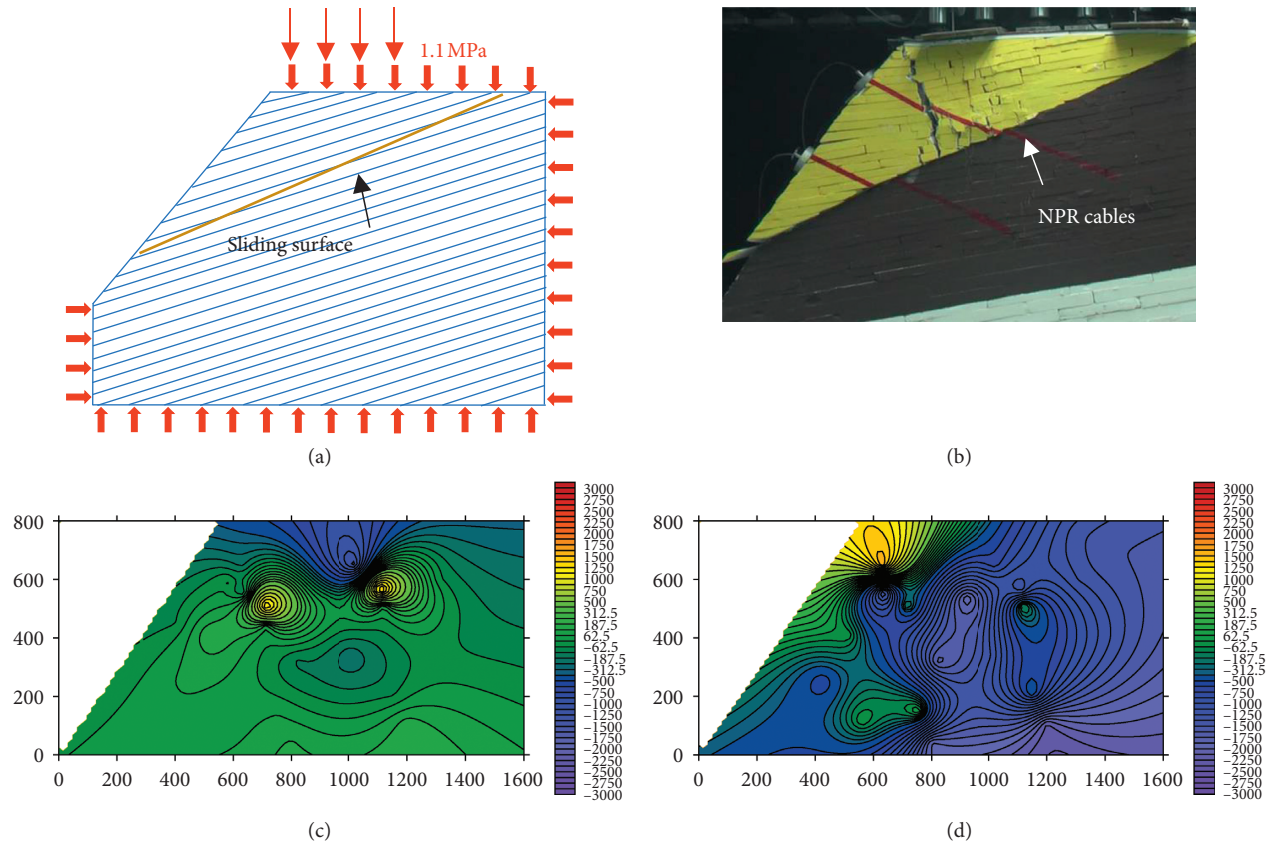

Figure 17: Fourth loading stage stable strain cloud map. (a) Model loading diagram. (b) Model loading variation diagram. (c) X-directional strain cloud map. (d) Y-directional strain cloud map.

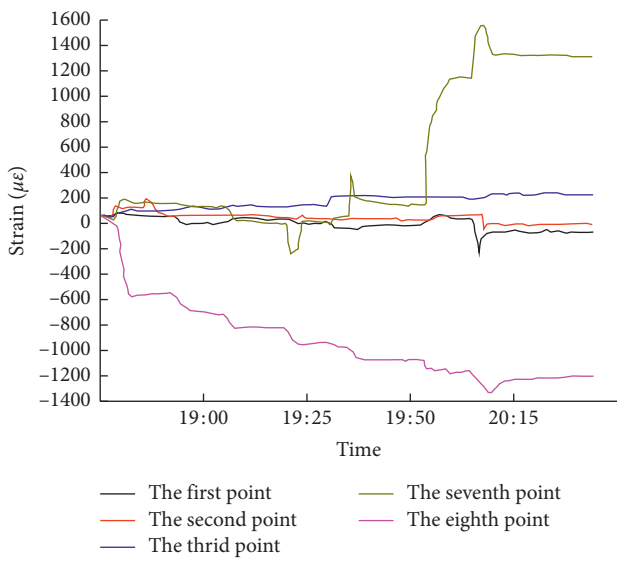

Figure 18: Curve of horizontal strain versus time at each key point.

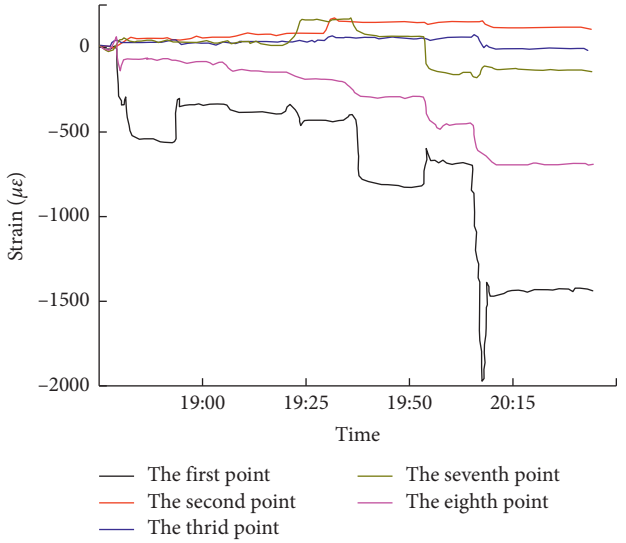

Figure 19: Vertical strain versus time curve for each key point.

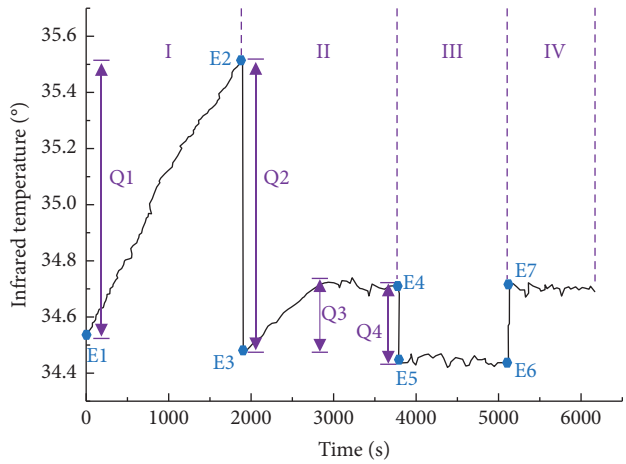

Figure 20: Infrared temperature curves vs time.

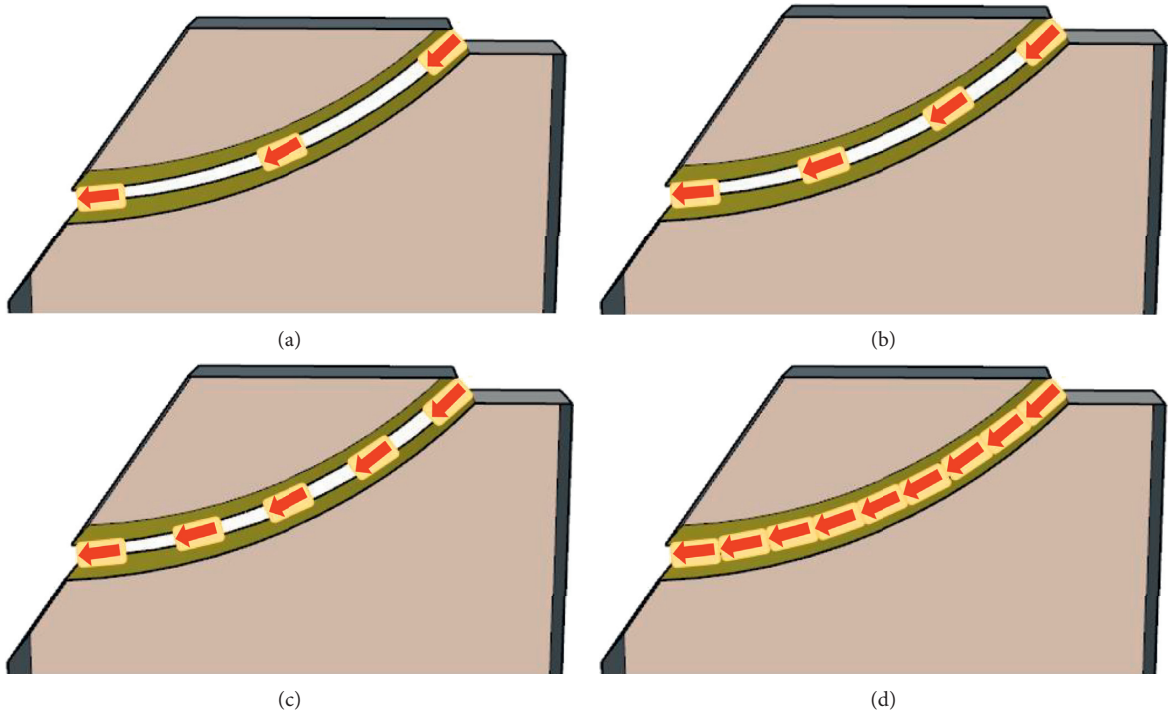

Figure 21: Changes in the sliding surface after loading at each stage. (a) Slip surface generation. (b) Slip surface extension. (c) The sliding surface continues to expand. (d) Penetration of sliding surface.

body expands more seriously than that in the second loading stage, and the energy is released before a large amount of agglomeration, so the infrared temperature curve has a small fluctuation range. After 30 minutes, stage IV loading (1.1 MPa) was carried out. The continued loading causes the sliding surface inside the sliding body to penetrate, and the sliding body transforms into a moving state and slips along the sliding surface. At this time, the temperature rises E7 – E6 = 0.2°C, and the main cause of the temperature rise is the friction between the sliding body and the sliding surface. The change in the sliding surface after loading in each stage of Figure 21 can clearly show the entire process of the sliding surface of the landslide from generation to extension to final penetration during the step-by-step loading process.

5. Conclusions

(1) According to the relationship between displacement and time, the maximum displacement of the upper part of the sliding body is 26 mm, and no obvious sliding occurs. In subsequent tests, a friction reducing pad can be used for all sliding surfaces (except for the slope foot at 10 cm).

(2) As load increases, the working resistance of the constant resistance large deformation anchor cable increases continuously, and the maximum measured sliding force is 420 N and 630 N, respectively, and the sliding body is destroyed. The transverse resistance communication cable has a high tensile strength, which causes the upper sliding body to not resist sliding. This also proves that the constant resistance large deformation anchor cable can play a significant role in stabilizing the slope.

(3) The gypsum board strain in the lower part of the sliding body is larger than other positions (the horizontal maximum strain is 1400 $\mu\varepsilon$; the vertical maximum strain is 2000 $\mu\varepsilon$), so the gypsum board here is relatively broken, which may be because the gypsum board used in the test is incomplete or uneven, increasing the crack of the sliding body itself. The smoothness of the surface of the sliding body should be ensured during the test to facilitate sliding of the sliding body.

(4) Analysis of the relationship between infrared temperature and time shows that the increase of temperature is mainly because the interaction force between the element plates is converted into variable performance and agglomerates between the element plates, and the temperature change caused by the first loading is the largest. Slippage and cracking are the primary energy release mechanisms. The gypsum unit plate used in the test is a viscoelastic body rather than a rigid body, so the rock layer is prone to plastic deformation when under load, and storing large amounts of elastic energy is difficult.

Data Availability

The data used to support the findings of this study are available from the corresponding author upon request.

Conflicts of Interest

The authors declare that there are no conflicts of interest regarding the publication of this paper.

Acknowledgments

This study was supported by the Zhejiang Province Key R&D Projects (No. 2019C03104) and the Fundamental Research Funds for the Central Universities, SCUT (No. 2015QB02).

References

[1] C. Zhu, Z. G. Tao, and S. Zhao, "V shaped gully method for controlling rock fall of high-steep slope in China," *Bulletin of Engineering Geology and the Environment*, vol. 78, no. 4, pp. 2731–2747, 2019.

[2] J. Xu, A. Haque, W. Gong, and R. P. Gamage, "Experimental study on the bearing mechanisms of rock-socketed piles in soft rock based on micro X-ray CT analysis," *Rock Mechanics and Rock Engineering*, vol. 53, no. 8, pp. 3395–3416, 2020.

[3] H. Y. Pan, D. W. Yin, N. Jiang, and Z. G. Xia, "Crack initiation behaviors of granite specimens containing crossing-double-flaws with different lengths under uniaxial loading," *Advances in Civil Engineering*, vol. 2020, Article ID 8871335, 13 pages, 2020.

[4] J. B. Xu, H. Li, K. Du, and C. G. Yan, "Field investigation of force and displacement within a strata slope using a real-time remote monitoring system," *Environmental Earth Sciences*, vol. 77, no. 15, 2018.

[5] Z. G. Tao, C. Zhu, X. H. Zheng, and M. C. He, "Slope stability evaluation and monitoring of Tonglushan ancientcopper mine relics," *Advances in Mechanical Engineering*, vol. 10, no. 8, 2018.

[6] G. Feng, X. C. Wang, M. Wang, and Y. Kang, "Experimental investigation of thermal cycling effect on fracture characteristics of granite in a geothermal-energy reservoir," *Engineering Fracture Mechanics*, vol. 235, pp. 1–16, Article ID 107180, 2020.

[7] H. Rahardjo and A. Satyanaga, "Sensing and monitoring for assessment of rainfall-induced slope failures in residual soil," *Proceedings of the Institution of Civil Engineers - Geotechnical Engineering*, vol. 172, no. 6, pp. 496–506, 2019.

[8] Q. B. Zhan, X. J. Sun, C. Li, Y. W. Zhao, and X. J. Zhou, "Stability analysis and reinforcement of a high-steep rock slope with faults: numerical analysis and field monitoring," *Advances in Mechanical Engineering*, vol. 2019, Article ID 3732982, 8 pages, 2019.

[9] C. Zhou, Q. Jiang, W. Wei, Y. Chen, and G. Rong, "Safety monitoring and stability analysis of left bank high slope at Jinping-I hydropower station," *Quarterly Journal of Engineering Geology and Hydrogeology*, vol. 49, no. 4, pp. 308–321, 2016.

[10] C. X. Wang, B. T. Shen, J. T. Chen, and W. X. Tong, "Compression characteristics of filling gangue and simulation of mining with gangue backfilling: an experimental investigation," *Geomechanics and Engineering*, vol. 20, no. 6, pp. 485–495, 2020.

[11] G. C. Shi, X. J. Yang, and H. C. Yu, "Acoustic emission characteristics of creep fracture evolution in double-fracture fine sandstone under uniaxial compression," *Engineering Fracture Mechanics*, vol. 210, pp. 13–28, 2019.

[12] H. Pei, S. Zhang, L. Borana, Y. Zhao, and J. Yin, "Slope stability analysis based on real-time displacement measurements," *Measurement*, vol. 131, pp. 686–693, 2019.

[13] Y. I. Kolesnikov, M. M. Nemirovich-Danchenko, S. V. Goldin, and V. S. Seleznev, "Slope stability monitoring from microseismic field using polarization methodology," *Natural Hazards and Earth System Sciences*, vol. 3, no. 6, pp. 515–521, 2003.

[14] M. Sundermeier and C. Schlenke, "Projektallianzen für Großbauvorhaben-lediglich "noch ein Partnerschaftsmodell" oder Paradigmenwechsel der Vertragsgestaltung?" *Bautechnik*, vol. 87, no. 9, pp. 562–571, 2010.

[15] G. F. Song, J. M. Du, J. Ke, and Q. Deng, "Stability limit analysis of bedding rock slopes based on pseudo-dynamic method," *China Earthquake Engineering Journal*, vol. 41, no. 4, pp. 931–938, 2019.

[16] O. Hungr, S. Leroueil, and L. Picarelli, "The Varnes classification of landslide types, an update," *Landslides*, vol. 11, no. 2, pp. 167–194, 2014.

[17] W. Hao and X. M. Zhang, "Remote sensing interpretation of geological disaster in chongqing city of China," *Disaster Advances*, vol. 6, pp. 289–295, 2013.

[18] R. Stone, "Disaster relief: too late, earth scans reveal the power of a killer landslide," *Science*, vol. 311, no. 5769, pp. 1844-1845, 2006.

[19] F. L. Wang, C. H. Liu, and Z. Gong, "Mechanisms of bolt support for bedding rock slopes," *Chinese Journal of Rock Mechanics and Engineering*, vol. 33, no. 7, pp. 1465–1470, 2014.

[20] R. G. Deng, D. P. Zhou, A. H. Li, and K. Wang, "On the critical length of unstable rock stratum on bedrock slope," *Chinese Jounal of Geotechnical Engineering*, vol. 24, no. 2, pp. 178–182, 2002.

[21] J. Y. Dong, G. X. Yang, F. Q. Wu, and S. W. Qi, "The large-scale shaking table test study of dynamic response and failure mode of bedding rock slope under earthquake," *Rock and Soil Mechanics*, vol. 32, no. 10, pp. 2977–2982, 2011.

[22] W. Lu, B. Bai, and C. X. Chen, "Analysis of mechanism of plane sliding failure for bedded rock slopes," *Rock and Soil Mechanics*, vol. 32, no. S2, pp. 204–207, 2011.

[23] R. Q. Huang, "Large-scale landslides and their sliding mechanisms in China since the 20th century," *Chinese Journal of Rock Mechanics and Engineering*, vol. 26, no. 3, pp. 433–454, 2007.

[24] L. Zan, G. Latini, and E. Piscina, "Landslides early warning monitoring system," in *IEEE International Geoscience and Remote Sensing Symposium (IGARSS 2002)/24th Canadian Symposium on Remote Sensing*, Toronto, Canada, June 2002.

[25] B. A. Reevea, G. F. Stickley, and D. A. Noon, "Developments in monitoring mine slope stability using radar interferometry," in *IEEE International Geoscience and Remote Sensing Symposium*, Honolulu, HI, USA, August 2000.

[26] R. Ohbayashi, Y. Nakajima, and H. Nishikado, "Monitoring system for landslide disaster by wireless sensing node network," in *Annual Conference of the SICE*, Chofu, Japan, September 2008.

[27] R. Tang, J. L. Wang, and X. M. Fan, "Application of TDR technology to landslides monitoring," *Journal of Geological Hazards and Environment Preservation*, vol. 18, no. 1, pp. 105–110, 2007.

[28] P. Zhang, M. C. He, Z. G. Tao, and B. Zhang, "Modification on sliding perturbation remote monitoring system and its application effect analysis," *Chinese Journal of Rock Mechanics and Engineering*, vol. 30, no. 10, pp. 2026–2032, 2011.

[29] G. L. Zu, "Instability mechanism of bedding slope of opencast coal mine stratified rock mass and control mining technology," *Safety of Coal Mines*, vol. 48, no. 5, pp. 98–102, 2017.

[30] N. Wu, Z. Z. Liang, J. R. Zhou, and Y. Z. Zhang, "Energy evolution characteristics of coal specimens with preformed holes under uniaxial compression," *Geomechanics and Engineering*, vol. 20, no. 1, pp. 55–66, 2020.

[31] F. Ren, C. Zhu, and M. He, "Moment tensor analysis of acoustic emissions for cracking mechanisms during schist strain burst," *Rock Mechanics and Rock Engineering*, vol. 53, no. 1, pp. 153–170, 2020.

[32] W. Z. Han, Z. F. Zhang, S. D. Wu, and S. X. Li, "Investigation on the geometrical aspect of deformation during equal-channel angular pressing by in-situ physical modeling experiments," *Materials Science & Engineering A*, vol. 476, no. 1-2, pp. 224–229, 2008.

[33] Q. Zhao, J. Guo, S. L. Hao, and J. H. Geng, "Experiments of physical modeling for petrophysical properties of natural gas hydrate," *Chinese Journal of Geophysics*, vol. 48, no. 3, pp. 649–655, 2005.

[34] L. K. Morgan, L. Stoeckl, A. D. Werner, and V. E. A. Post, "An assessment of seawater intrusion overshoot using physical and numerical modeling," *Water Resources Research*, vol. 49, no. 10, pp. 6522–6526, 2013.

[35] J. Wang, Y. Zhang, Z. Qin, S. G. Song, and P. Lin, "Analysis method of water inrush for tunnels with damaged water-resisting rock mass based on finite element method-smooth particle hydrodynamics coupling," *Computers and Geotechnics*, vol. 126, 2020.

[36] B. Chen, S. C. Zhang, Y. Y. Li, Z. K. Li, and H. J. Zhou, "Physical simulation study of crack propagation and instability information discrimination of rock-like materials with faults[J]," *Arabian Journal of Geosciences*, vol. 13, 2020.

[37] J. T. Chen, J. H. Zhao, S. C. Zhang, Y. Zhang, and F. Yang, "An experimental and analytical research on the evolution of mining cracks in deep floor rock mass," *Pure and Applied Geophysics*, vol. 177, no. 11, pp. 5325–5348, 2020.

[38] C. Zhu, M. He, M. Karakus, X. Cui, and Z. Tao, "Investigating toppling failure mechanism of anti-dip layered slope due to excavation by physical modelling," *Rock Mechanics and Rock Engineering*, vol. 53, no. 11, pp. 5029–5050, 2020.

[39] D. K. Liu, Z. L. Gu, R. X. Liang, J. W. Su, and D. Z. Ren, "Impacts of pore-throat system on fractal characterization of tight sandstones," *Geofluids*, vol. 2020, no. 9, 17 pages, Article ID 4941501, 2020.

[40] X. Wang, C. Liu, S. Chen, L. Chen, and K. Li, "Impact of coal sector's de-capacity policy on coal price," *Applied Energy*, vol. 265, 2002.